Pre-print version accepted for publication in the proceedings of the 2023 International Symposium on Medical Robotics (ISMR), Atlanta GA

Modeling Tendon-actuated Concentric Tube Robots

Yash Chitalia, Abdulhamit Donder, and Pierre E. Dupont, *Fellow, IEEE*

***Abstract*— Mechanics-based models have been developed to describe the shape of tendon-actuated continuum robots. Models have also been developed to describe the shape of concentric tube robots, i.e., nested combinations of precurved superelastic tubes. While an important class of continuum robots used in endoscopic and intracardiac medical applications combines these two designs, existing models do not cover this combination. Tendon-actuated models are limited to a single tube while concentric tube models do not include tendon-produced forces and moments. This paper derives a mechanics-based model for this hybrid design and assesses it using numerical and physical experiments involving a pair of tendon-actuated tubes. It is demonstrated that, similar to concentric tube robots, relative twisting between the tendon-actuated tubes is an important factor in determining overall robot shape.**

I. Introduction

The flexibility and small cross section of continuum robot designs make them highly effective for performing minimally invasive medical procedures, e.g., in the airways, bowel, vasculature and urinary tract [1], [2]. Tendon-actuated tubular designs are typically used since they are capable of producing very high tip curvatures with long flexible proximal sections. They also provide a large central lumen for delivering tools and sensors. These devices can be inserted into a body lumen such that the steerable tip is used to guide navigation through the body while also enabling tip positioning to perform diagnostic and therapeutic tasks. The proximal portion of the robot transmits longitudinal forces for insertion and retraction while flexing laterally to follow the contours of the body lumen.

While a single tendon-actuated tip section can provide sufficient steerability in some applications, other clinical interventions require more degrees of freedom. These can be provided by creating telescoping sets of tendon-actuated tubes (Fig. 1). Such designs are comparable to concentric tube robots except that the curvature of each tube has not been pre-set, but is instead actively controlled by tendon tension. Such telescoping designs are used, for example, in transcatheter electrophysiology procedures [3], peripheral artery disease [4], [5], and in transcatheter heart valve repair [6]. They are also used in endoscopic peripheral lung procedures [7].

Modeling the shape of tendon-actuated robots has produced a rich literature as reviewed in [8]. While in some situations, an assumption of constant curvature is appropriate [9], it has also been demonstrated that off-axis loading can produce robot twisting which invalidates this assumption [10]. Accordingly, several researchers have developed tendon-actuation models that allow curvature to vary with arc length [10]–[12]. Tube twisting has similarly been shown to be important in modeling concentric tube robots where the pre-curved tubes produce off-axis loading on each other and so exhibit relative twist [13], [14].

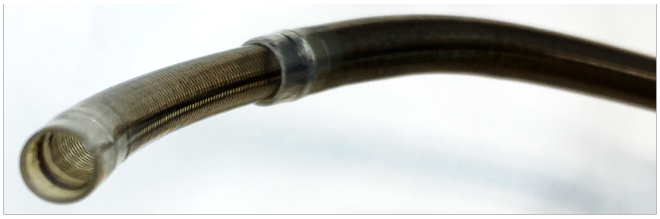

Fig. 1: Telescoping two-tube tendon-actuated catheter.

While the tendon-actuation models [10]–[12] are versatile in providing for arbitrary arrangements and numbers of tendons, they are formulated for the case in which all tendons actuate a single flexural structure. There are also models for multi-section tendon-actuated designs in which each section can extend and retract to a certain extent relative to its proximal section [15], [16]. These designs, however, are constructed with concentric central backbones and spacer disks. Each tendon passes through the spacer disks of all proximal sections constraining the sections to twist together as a single structure. Consequently, neither the single-section models of [10]–[12] nor the multi-section models of [15], [16] consider twisting between telescoping sections.

The contribution of this paper is to introduce a hybrid formulation that can be applied to nested combinations of tendon-actuated tubes in which each tube and its tendons can twist and translate freely relative to the others. The model is derived in the next section. A detailed evaluation is then provided for a pair of tendon-actuated tubes. Simulation is used to evaluate the effect on robot shape that arises due to relative twisting of the two tubes. Experiments are then presented to assess the accuracy of the model in predicting robot shape. Conclusions and future directions are presented in the final section of the paper.

II. Mechanics-based Model

Our formulation is based on modeling the tubes and tendons as Cosserat rods and strings, respectively, following the approach of [10]. The individual tube models are combined in manner similar to [13] in which compatibility conditions constrain the overlapping tubes to share a common center line. As with these prior models, a linear constitutive model

This work was supported by the NIH under grant R01HL124020. Yash Chitalia is with the Healthcare Robotics and Telesurgery (HeaRT) Laboratory, University of Louisville, Louisville, Kentucky, USA. Abdulhamit Donder and Pierre E. Dupont are with the Department of Cardiovascular Surgery, Boston Children's Hospital, Harvard Medical School, Boston, Massachusetts, USA.

Yash Chitalia is the corresponding author {yash.chitalia@louisville.edu}.

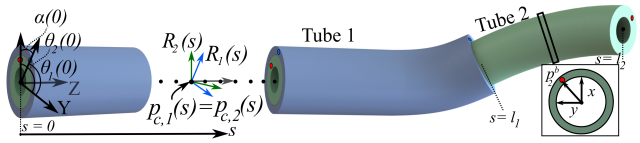

Fig. 2: Mechanical model of telescoping tendon-driven tubes and the associated twist angles, θ_i (inset shows the cross-section and the location of the tendon for the inner tube, 'Tube 2'). The reference frame labeled with capital letters is the world reference frame.

is assumed and friction between the tendons and the tubes as well as between the tubes is assumed negligible. In this work, we assume a total of two tubes, each tube possessing a single tendon which runs in a straight channel along the tube. External forces and moments are omitted. These simplifications are made for convenience and are not limitations of the approach.

A. Tube Kinematics

The differential equation describing the center line of tube i as a function of arc length, s, is given as

$$\dot{p}_{c,i}(s) = R_i(s)v_i(s) \quad \dot{R}_i(s) = R_i(s)[u_i(s)] \tag{1}$$

where $R_i(s) \in SO(3)$ is the material frame orientation with the z axis directed along the center line tangent and the x and y axes defining the cross sectional plane, as shown in Fig. 2. The angle, $\theta_i(s)$, denotes the rotation of the body coordinate frame about the z axis with respect to a reference frame at the base. This angle is comprised of components due to rigid body rotation of the tube at its base as well as twisting deformation along its length.

Center line position is given by $p_{c,i},(s) \in \mathbb{R}^3$ with respect to a fixed global frame, $v_i(s) \in \mathbb{R}^3$ is the linear strain rate, and $u_i(s) \in \mathbb{R}^3$ is the angular strain. For any vector in $\mathbb{R}^3$, the bracket notation $[.]$ indicates the corresponding skew symmetric matrix and derivatives with respect to arc length are denoted by $\dot{q} = {}^{dq}/_{ds}$. In the following, dependence on arc length is dropped for brevity, e.g., $q(s)$ is written as q.

B. Equilibrium Equations

For a special Cosserat rod with internal forces and moments indicated by vectors $n \in \mathbb{R}^3$ and $m \in \mathbb{R}^3$ respectively, and applied forces and moments per unit length given by $f \in \mathbb{R}^3$ and $\tau \in \mathbb{R}^3$ respectively, the equations for static equilibrium are indicated in [13] as

$$\begin{bmatrix} \dot{n}_i \\ \dot{m}_i \end{bmatrix} = \begin{bmatrix} [u_i] & 0 \\ [v_i] & [u_i] \end{bmatrix} \begin{bmatrix} n_i \\ m_i \end{bmatrix} + \begin{bmatrix} f_i \\ \tau_i \end{bmatrix} \tag{2}$$

C. Constitutive Model

For each tube, shear force can be related to shear strain and bending moment to curvature using a constitutive model. Assuming a linear relationship,

$$\begin{bmatrix} n_i \\ m_i \end{bmatrix} = \begin{bmatrix} K_{se,i} & 0 \\ 0 & K_{bt,i} \end{bmatrix} \begin{bmatrix} v_i - v_i^* \\ u_i - u_i^* \end{bmatrix} \tag{3}$$

and,

$$K_{se,i} = \begin{bmatrix} GA_i & 0 & 0 \\ 0 & GA_i & 0 \\ 0 & 0 & EA_i \end{bmatrix}, \tag{4}$$

$$K_{bt,i} = \begin{bmatrix} EI_{xx,i} & 0 & 0 \\ 0 & EI_{yy,i} & 0 \\ 0 & 0 & GJ_{zz,i} \end{bmatrix} \tag{5}$$

where, u_i^* is the initial value of angular strain rate, v_i^* is the initial linear strain rate, G is the shear modulus, E is the modulus of elasticity, I_{xx} and I_{yy} are the second moments of area about the local frame axes, while J_{zz} is the corresponding polar moment of area.

D. Distributed Forces and Moments

The distributed forces, f_i and moments, τ_i, applied to each tube are comprised of three components generated by the tendons, adjacent tubes and external loads, respectively.

$$f_i = f_{t,i} + f_{c,i} + f_{e,i}, \tag{6}$$

$$\tau_i = \tau_{t,i} + \tau_{c,i} + \tau_{e,i} \tag{7}$$

Given our assumption that tendons follow a straight path along each tube, tendon position in the cross-sectional body frame as $p_i^b = [x_i, y_i, 0]^T$. Following [10], the distributed force and moment components due to scalar tendon tension, λ_i are given by

$$f_{t,i} = -\lambda_i \frac{[\dot{p}_i^b]^2}{||\dot{p}_i^b||^3}\ddot{p}_i^b, \quad \tau_{t,i} = -[p_i^b]f_{t,i} = -[p_i^b]\lambda_i \frac{[\dot{p}_i^b]^2}{||\dot{p}_i^b||^3}\ddot{p}_i^b \tag{8}$$

where the derivatives of tendon position may be expressed (in the body frame) as follows:

$$\dot{p}_i^b = [u_i]p_i^b + v_i, \quad \ddot{p}_i^b = [u_i]\dot{p}_i^b - [p_i^b]\dot{u}_i + \dot{v}_i \tag{9}$$

Assuming negligible friction, the tubes apply equal and opposite interaction forces to each other that act through the common center line. Consequently, no moments are produced, $\tau_{c,i} = 0$. Assuming no external loading, $f_{e,i} = \tau_{e,i} = 0$. Consequently, (6) and (7) reduce to

$$f_i = f_{t,i} + f_{c,i}, \quad \tau_i = \tau_{t,i} \tag{10}$$

E. Compatibility Constraints

Since overlapping tubes share a common center line, their bending curvature, $u_i|_{(x,y)}$ must be equal when expressed in the same coordinate frame. Furthermore, their cross-sectional shear strain, $v_i|_{(x,y)}$ must also be equal. As shown below for two tubes, these constraints reduce the state variables to be integrated to those of a single tube, e.g., $\{u_1, v_1\}$, plus the z components for the other tubes, $\{u_{i,z}, v_{i,z}\},\ i \in 2, \ldots, n$, assuming a total of n tubes.

Furthermore, $u_{i,z}$ can be represented in terms of the relative twist rate between tubes. Considering two tubes, the relative rotation angle between the tubes is given by $\alpha(s) = \theta_2(s) - \theta_1(s)$ (see Fig. 2) and the derivatives of this relationship is $\dot{\alpha}(s) = u_{2,z}(s) - u_{1,z}(s)$ and $\ddot{\alpha} = \dot{u}_{2,z} - \dot{u}_{1,z}$. The curvature compatibility condition can now be expressed as

$$u_2(s) = R_z^T(\alpha)u_1(s) + \dot{\alpha}(s)e_3 \tag{11}$$

where $e_3 = [0, 0, 1]^T$ and $R_z(\alpha)$ is defined as a rotation about the z-axis between the two body frames, such that $R_2 = R_1 R_z(\alpha)$. Differentiating with respect to arc-length

$$\dot{u}_2 = R_z^T(\alpha)\dot{u}_1 + \frac{dR_z^T(\alpha)}{d\alpha}\dot{\alpha}u_1 + \ddot{\alpha}e_3 \tag{12}$$

$$= (R_z^T(\alpha) - e_{(3,3)})\dot{u}_1 + \dot{\alpha}[e_3]^T R_z^T(\alpha)u_1 + e_3\dot{u}_{2,z} \tag{13}$$

Since the term $\ddot{\alpha}e_3$ can be rewritten as

$$\ddot{\alpha}e_3 = e_3\dot{u}_{2,z} - e_{(3,3)}\dot{u}_1 \tag{14}$$

where $e_{(3,3)} = \text{diag}(e_3)$ is a diagonal matrix with e_3 forming its diagonal elements. Considering shear strain now, compatibility produces the following constraint

$$v_2|_{x,y} = R_z^T(\alpha)v_1\Big|_{x,y} \tag{15}$$

Similar to the relationship for the angular strain rates, introducing a parameter, $\dot{\beta} = v_{2,z} - v_{1,z}$, results in the following relationship

$$\dot{v}_2 = R_z^T(\alpha)\dot{v}_1 + \dot{\alpha}[e_3]^T R_z^T(\alpha)v_1 + \ddot{\beta} \tag{16}$$

F. Model Equations

The remaining challenge in formulating the model is that the distributed forces on the tubes, f_i, in Eq. (2) include the unknown tube-on-tube reaction forces, $f_{c,i}$, in Eq. (10). Since these forces occur as equal and opposite pairs when considering all of the tubes, they can be eliminated by summing the equilibrium equation, Eq. (2), over all of the tubes. The sum of moment components for two tubes is

$$\begin{aligned}&\dot{m}_1 + R_z(\alpha)\dot{m}_2 + [u_1]m_1 \\ &+ \{[u_1]R_z(\alpha) + \dot{\alpha}R_z(\alpha)[e_3]\}m_2 + [v_1]n_1 \\ &+ R_z(\alpha)[v_2]n_2 + \tau_{t,1} + R_z(\alpha)\tau_{t,2}|_{x,y} = 0\end{aligned} \tag{17}$$

Substituting the constitutive model of Eq. (3) and the distributed moments from the tendons, Eq. (8), results in an expression involving only curvatures and shear strains,

$$\begin{aligned}&K_{bt,1}(\dot{u}_1 - \dot{u}_1^*) + R_z(\alpha)K_{bt,2}(\dot{u}_2 - u_2^*) \\ &+ [u_1]K_{bt,1}(u_1 - u_1^*) \\ &+ \{[u_1]R_z(\alpha) + \dot{\alpha}R_z(\alpha)[e_3]\}K_{bt,2}(u_2 - u_2^*) \\ &+ [v_1]K_{se,1}(v_1 - e_3) \\ &+ R_z(\alpha)[v_2]K_{se,2}(v_2 - e_3) - [p_1^b]\lambda_1\frac{[\dot{p}_1^b]^2}{||\dot{p}_1^b||^3}\ddot{p}_1^b \\ &- R_z(\alpha)[p_2^b]\lambda_2\frac{[\dot{p}_2^b]^2}{||\dot{p}_2^b||^3}\ddot{p}_2^b\Big|_{x,y} = 0\end{aligned} \tag{18}$$

Here, we assume $v_1^* = v_2^* = e_3$. Substituting for $\ddot{p}_i^b$ from Eq. (9) as well as the compatibility equations (11)-(16) allows the sum of moments equilibrium equation to be reduced to the form

$$\mathbb{G}_u\dot{u}_1 + \mathbb{G}_v\dot{v}_1 + \mathbb{G}_{u_2}\dot{u}_{2,z} + \mathbb{G}_{v_2}\dot{v}_{2,z}|_{x,y} = \mathbb{RHS}_{u_1}|_{x,y} \tag{19}$$

Here, the matrices themselves are functions of the state variables and are given by the following expressions in which $\alpha_1 = 0$ and $\alpha_2 = \alpha$ are used for compactness.

$$\begin{aligned}\mathbb{G}_u|_{x,y} = &-R_z(\alpha)K_{bt,2}e_{(3,3)} - \frac{\lambda_2}{||\dot{p}_2^b||^3}R_z(\alpha)[p_2^b][\dot{p}_2^b]^2[p_2^b]e_{(3,3)} \\ &+ \sum_{i=1}^{2} R_z(\alpha_i)\left(K_{bt,i} + \frac{\lambda_i}{||\dot{p}_i^b||^3}[p_i^b][\dot{p}_i^b]^2[p_i^b]\right)R_z^T(\alpha_i)\Big|_{x,y}\end{aligned} \tag{20}$$

$$\begin{aligned}&\mathbb{G}_v|_{x,y} \\ &= -\frac{\lambda_1}{||\dot{p}_1^b||^3}[p_1^b][\dot{p}_1^b]^2 - \frac{\lambda_2}{||\dot{p}_2^b||^3}R_z(\alpha)[p_2^b][\dot{p}_2^b]^2(R_z^T(\alpha) - e_{(3,3)})\Big|_{x,y}\end{aligned} \tag{21}$$

$$\mathbb{G}_{u_2}|_{x,y} = R_z(\alpha)K_{bt,2}e_3 + \frac{\lambda_2}{||\dot{p}_2^b||^3}R_z(\alpha)[p_2^b][\dot{p}_2^b]^2[p_2^b]e_3\Big|_{x,y} \tag{22}$$

$$\mathbb{G}_{v_2}|_{x,y} = -\frac{\lambda_2}{||\dot{p}_2^b||^3}R_z(\alpha)[p_2^b][\dot{p}_2^b]^2e_3\Big|_{x,y} \tag{23}$$

$$\begin{aligned}&\mathbb{RHS}_{u_1}|_{x,y} = K_{bt,1}\dot{u}_1^* + R_z(\alpha)K_{bt,2}\dot{u}_2^* \\ &- \frac{\dot{\alpha}\lambda_2}{||\dot{p}_2^b||^3}R_z(\alpha)[p_2^b][\dot{p}_2^b]^2[p_2^b][e_3]^T R_z^T(\alpha)u_1 \\ &- \dot{\alpha}R_z(\alpha)K_{bt,2}[e_3]^T R_z^T(\alpha)u_1 - [u_1]K_{bt,1}(u_1 - u_1^*) \\ &- [u_1]R_z(\alpha)K_{bt,2}(u_2 - u_2^*) - \dot{\alpha}R_z(\alpha)[e_3]K_{bt,2}(u_2 - u_2^*) \\ &- [v_1]K_{se,1}(v_1 - e_3) - R_z(\alpha)[v_2]K_{se,2}(v_2 - e_3) \\ &+ \frac{\lambda_1}{||\dot{p}_1^b||^3}[p_1^b][\dot{p}_1^b]^2[u_1]\dot{p}_1^b + \frac{\lambda_2}{||\dot{p}_2^b||^3}R_z(\alpha)[p_2^b][\dot{p}_2^b]^2[u_2]\dot{p}_2^b \\ &+ \frac{\lambda_2\dot{\alpha}}{||\dot{p}_2^b||^3}R_z(\alpha)[p_2^b][\dot{p}_2^b]^2[e_3]^T R_z^T(\alpha)v_1\Big|_{x,y}\end{aligned} \tag{24}$$

Equation (19) provide 2 equations which are linear in the derivatives of the 8 state variables, $\{\dot{u}_1, \dot{v}_1, \dot{u}_{2,z}, \dot{v}_{2,z}\}$. Two more scalar independent equations are obtained from the z component of the moment equilibrium equation for both tubes. For each of the individual tubes, $i = \{1, 2\}$, this scalar equation takes on the following form,

$$\{\dot{m}_i + [v_i]n_i + [u_i]m_i + \tau_i\}|_z = 0 \tag{25}$$

Substituting the constitutive model Eq. (3) and distributed tendon moments expression Eq. (8) yields

$$\begin{aligned}\{&K_{bt,i}(\dot{u}_i - \dot{u}_i^*) + [v_i]K_{se,i}(v_i - e_3) + [u_i]K_{bt,i}(u_i - u_i^*) \\ &- \frac{\lambda_i}{||\dot{p}_i^b||^3}[p_i^b][\dot{p}_i^b]^2\ddot{p}_i^b\}\Big|_z = 0\end{aligned} \tag{26}$$

For the outer tube, this reduces to the following:

$$(\mathbb{G}_u\dot{u}_1 + \mathbb{G}_v\dot{v}_1 + \mathbb{G}_{u_2}\dot{u}_{2,z} + \mathbb{G}_{v_2}\dot{v}_{2,z})|_z = \mathbb{RHS}_{u_1}|_z \tag{27}$$

The individual terms are as follows:

$$\mathbb{G}_u|_z = K_{bt,1} + \frac{\lambda_1}{||\dot{p}_1^b||^3}[p_1^b][\dot{p}_1^b]^2][p_1^b]\Big|_z \tag{28}$$

$$\mathbb{G}_v|_z = -\frac{\lambda_1}{||\dot{p}_1^b||^3}[p_1^b][\dot{p}_1^b]^2\Big|_z \tag{29}$$

$$\mathbb{G}_{u_2}|_z = 0, \quad \mathbb{G}_{v_2}|_z = 0 \tag{30}$$

$$\begin{aligned}\mathbb{RHS}_{u_1}|_z = &-\frac{\lambda_1}{||\dot{p}_1^b||^3}[p_1^b][\dot{p}_1^b]^2[u_1][p_1^b]u_1 \\ &- [u_1]K_{bt,1}(u_1 - u_1^*) + K_{bt,1}\dot{u}_1^* \\ &+ \frac{\lambda_1}{||\dot{p}_1^b||^3}[p_1^b][\dot{p}_1^b]^2[u_1]v_1 - [v_1]K_{se,1}(v_1 - e_3)\Big|_z\end{aligned} \tag{31}$$

Using Eqs. (9), (11), (16) in (25) for the inner tube we get the following scalar equation,

$$\text{row}_3(\mathbb{J}_u)\dot{u}_1 + \text{row}_3(\mathbb{J}_v)\dot{v}_1 + \mathbb{J}_{u_{2,z}}\dot{u}_{2,z} + \mathbb{J}_{v_{2,z}}\dot{v}_{2,z} = \mathbb{RHS}_{u_2} \tag{32}$$

in which row_3 extracts the third row of the matrix and $\mathbb{J}_u, \mathbb{J}_v, \mathbb{A}_{u,3}, \mathbb{A}_{v,3}$, $\mathbb{J}_{v_{2,z}}$ and $\mathbb{J}_{u_{2,z}}, \mathbb{B}_3 e_3 \in \Re$ are given by:

$$\mathbb{J}_u = \left[K_{bt,2} + \frac{\lambda_2}{||\dot{p}_2^b||^3}[p_2^b][\dot{p}_2^b]^2[p_2^b]\right](R_z^T(\alpha) - e_{(3,3)}) \tag{33}$$

$$\mathbb{J}_v = -\frac{\lambda_2}{||\dot{p}_2^b||^3}[p_2^b][\dot{p}_2^b]^2 R_z^T(\alpha) \tag{34}$$

$$\mathbb{J}_{u_{2,z}} = \left\{K_{bt,2}e_3 + \frac{\lambda_2}{||\dot{p}_2^b||^3}[p_2^b][\dot{p}_2^b]^2[p_2^b]e_3\right\}\Big|_z \tag{35}$$

$$\mathbb{J}_{v_{2,z}} = -\frac{\lambda_2}{||\dot{p}_2^b||^3}[p_2^b][\dot{p}_2^b]^2 e_3\Big|_z \tag{36}$$

and the right hand side terms can be elaborated as follows:

$$\begin{aligned}\mathbb{RHS}_{u_2} = &-\frac{\lambda_2}{||\dot{p}_2^b||^3}[p_2^b][\dot{p}_2^b]^2[u_2]\dot{p}_2^b - \dot{\alpha}K_{bt,2}[e_3]^T R_z^T u_1 \\ &- [u_2]K_{bt,2}(u_2 - u_2^*) - [v_2]K_{se,2}(v_2 - e_3) \\ &- \frac{\dot{\alpha}\lambda_2}{||\dot{p}_2^b||^3}[p_2^b][\dot{p}_2^b]^2[p_2^b][e_3]^T R_z^T u_1 \\ &+ \frac{\dot{\alpha}\lambda_2}{||\dot{p}_2^b||^3}[p_2^b][\dot{p}_2^b]^2[e_3]^T R_z^T v_1 - K_{bt,2}\dot{u}_2^*\Big|_z\end{aligned} \tag{37}$$

Now turning to the sum of shear strain components of the equilibrium equation (2), the same process can be repeated. Noting that the tube-on-tube distributed reaction forces, $f_{c,i}$, cancel by summing and substituting the constitutive model, (3), distributed tendon forces, (8), $\ddot{p}_i^b$ from (9) and compatibility equations (11)-(16) produces an expression of the form

$$\mathbb{H}_u\dot{u}_1 + \mathbb{H}_v\dot{v}_1 + \mathbb{H}_{u_2}\dot{u}_{2,z} + \mathbb{H}_{v_2}\dot{v}_{2,z}|_{(x,y)} = \mathbb{RHS}_2|_{(x,y)} \tag{38}$$

As with the moment equation (19), the coefficient matrices are functions of the state variables and are given by

$$\mathbb{H}_u|_{x,y} = \frac{\lambda_1}{||\dot{p}_1^b||^3}[\dot{p}_1^b]^2[p_1^b] + \frac{\lambda_2}{||\dot{p}_2^b||^3}R_z(\alpha)[\dot{p}_2^b]^2[p_2^b](R_z^T(\alpha) - e_{(3,3)})\Big|_{x,y} \tag{39}$$

$$\mathbb{H}_v|_{x,y} = K_{se,1} + R_z(\alpha)K_{se,2}R_z^T(\alpha) - \frac{\lambda_1}{||\dot{p}_1^b||^3}[\dot{p}_1^b]^2 - \frac{\lambda_2}{||\dot{p}_2^b||^3}R_z(\alpha)[\dot{p}_2^b]^2 R_z^T(\alpha)\Big|_{x,y} \tag{40}$$

$$\mathbb{H}_{u_2}|_{x,y} = \frac{\lambda_2}{||\dot{p}_2^b||^3}R_z(\alpha)[\dot{p}_2^b]^2[p_2^b]e_3\Big|_{x,y} \tag{41}$$

$$\mathbb{H}_{v_2}|_{x,y} = R_z(\alpha)K_{se,2}e_3 - \frac{\lambda_2}{||\dot{p}_2^b||^3}R_z(\alpha)[\dot{p}_2^b]^2 e_3\Big|_{x,y} \tag{42}$$

$$\begin{aligned}\mathbb{RHS}_{v_1}|_{x,y} = &-\frac{\dot{\alpha}\lambda_2}{||\dot{p}_2^b||^3}R_z(\alpha)[\dot{p}_2^b]^2[p_2^b][e_3]^T R_z^T(\alpha)u_1 \\ &- \frac{\dot{\alpha}\lambda_2}{||\dot{p}_2^b||^3}R_z(\alpha)[\dot{p}_2^b]^2[e_3]^T R_z^T(\alpha)v_1 \\ &+ \frac{\lambda_2}{||\dot{p}_2^b||^3}R_z(\alpha)[\dot{p}_2^b]^2[u_2]\dot{p}_2^b + \frac{\lambda_1}{||\dot{p}_1^b||^3}[\dot{p}_1^b]^2[u_1]\dot{p}_1^b \\ &- (\dot{\alpha}[e_3] - [u_1])R_z(\alpha)K_{se,2}(v_2 - e_3) \\ &- [u_1]K_{se,1}(v_1 - e_3) - \dot{\alpha}R_z(\alpha)K_{se,2}[e_3]^T R_z^T(\alpha)v_1\Big|_{x,y}\end{aligned} \tag{43}$$

From (38), we get 2 equations that are linear in the derivatives of our 8 state variables. Similar to the moment equations, we get the remaining two scalar equations corresponding to the independent extension of the individual tubes, $i = \{1, 2\}$, as follows,

$$\dot{n}_i + [u_i]n_i + f_i = 0 \tag{44}$$

For the outer tube, using the constitutive model and the expression for f_1 from Eq. (8), we get the following,

$$\mathbb{H}_u|_z = \frac{\lambda_1}{||\dot{p}_1^b||^3}[\dot{p}_1^b]^2[p_1^b]\Big|_z \tag{45}$$

$$\mathbb{H}_v|_z = (K_{se,1} - \frac{\lambda_1}{||\dot{p}_1^b||^3})[\dot{p}_1^b]^2\Big|_z \tag{46}$$

$$\mathbb{RHS}_{v_1}|_z = \frac{\lambda_1}{||\dot{p}_1^b||^3}[\dot{p}_1^b]^2[u_1]\dot{p}_1^b - [u_1]K_{se,1}(v_1 - e_3)\Big|_z \tag{47}$$

Similarly for the inner tube, we have the following linear scalar equation:

$$\text{row}_3(\mathbb{K}_u)\dot{u}_1 + \text{row}_3(\mathbb{K}_v)\dot{v}_1 + \mathbb{K}_{u_{2,z}}\dot{u}_{2,z} + \mathbb{K}_{v_{2,z}}\dot{v}_{2,z} = \mathbb{RHS}_{v_2} \tag{48}$$

$$\mathbb{K}_u = \frac{\lambda_2}{||\dot{p}_2^b||^3}[\dot{p}_2^b]^2[p_2^b](R_z(\alpha)^T - e_{(3,3)}) \tag{49}$$

$$\mathbb{K}_v = (K_{se,2} - \frac{\lambda_2}{||\dot{p}_2^b||^3}[\dot{p}_2^b]^2)(R_z(\alpha)^T - e_{(3,3)}) \tag{50}$$

$$\mathbb{K}_{u_{2,z}} = \frac{\lambda_2}{||\dot{p}_2^b||^3}[\dot{p}_2^b]^2[p_2^b]e_3\Big|_z \tag{51}$$

$$\mathbb{K}_{v_{2,z}} = K_{se,2}e_3 - \frac{\lambda_2}{||\dot{p}_2^b||^3}[\dot{p}_2^b]^2 e_3\Big|_z \tag{52}$$

$$\begin{aligned}\mathbb{RHS}_{v_2} = &\frac{\lambda_2}{||\dot{p}_2^b||^3}[\dot{p}_2^b]^2[u_2]\dot{p}_2^b - \frac{\dot{\alpha}\lambda_2}{||\dot{p}_2^b||^3}[\dot{p}_2^b]^2[p_2^b][e_3]^T R_z(\alpha)^T u_1 \\ &+ \frac{\dot{\alpha}\lambda_2}{||\dot{p}_2^b||^3}[\dot{p}_2^b]^2[e_3]^T R_z(\alpha)^T v_1 - [u_2]K_{se,2}(v_2 - e_3) \\ &- \dot{\alpha}K_{se,2}[e_3]^T R_z(\alpha)^T v_1\end{aligned} \tag{53}$$

Finally, we can combine (19), (38), (32) and (48), to express our final differential equation as:

$$\begin{bmatrix}\mathbb{G}_u & \mathbb{G}_v & \mathbb{G}_{u_{2,z}} & \mathbb{G}_{v_{2,z}} \\ \mathbb{H}_u & \mathbb{H}_v & \mathbb{H}_{u_{2,z}} & \mathbb{H}_{v_{2,z}} \\ \text{row}_3(\mathbb{J}_u) & \text{row}_3(\mathbb{J}_v) & \mathbb{J}_{u_{2,z}} & \mathbb{J}_{v_{2,z}} \\ \text{row}_3(\mathbb{K}_u) & \text{row}_3(\mathbb{K}_v) & \mathbb{K}_{u_{2,z}} & \mathbb{K}_{v_{2,z}}\end{bmatrix}\begin{bmatrix}\dot{u}_1 \\ \dot{v}_1 \\ \dot{u}_{2,z} \\ \dot{v}_{2,z}\end{bmatrix} = \begin{bmatrix}\mathbb{RHS}_{u_1} \\ \mathbb{RHS}_{v_1} \\ \mathbb{RHS}_{u_2} \\ \mathbb{RHS}_{v_2}\end{bmatrix} \tag{54}$$

G. Numerical solution

Equation (54) can be solved by inverting the matrix on the left side at each step. The kinematic inputs consist of the

tendon tensions, λ_1 and λ_2 along with the relative rotation angle of the tubes at their base, $\alpha(0)$. In addition, the relative axial displacement of the tubes determines the extended free length of the inner tube for which the model reduces to that of [10]. Boundary conditions at the base consist of the orientation and position $R(0)$, $p(0)$. Point forces and moments are generated at the distal ends of the tendons, e.g., $s = l_i$ for tubes $i = \{1, 2\}$, and applied to the tubes through which the tendons run [10]. These are given by

$$F_i^b(l_i) = -\frac{\lambda_i}{||\dot{p}_i^b(l_i)||} R_z(\alpha_i)\dot{p}_i^b(l_i) \tag{55}$$

$$\mathrm{T}_i^b(l_i) = -\frac{\lambda_i}{||\dot{p}_i^b(l_i)||} R_z(\alpha_i)[p_i^b(l_i)]\dot{p}_i^b(l_i) \tag{56}$$

The boundary condition at the tip of the outer tube ($s = l_1$), is therefore given by,

$$\sum_{i=1}^{2} R_z(\alpha_i)K_{bt,i}(u_i(l_1^-) - u_i^*) = \mathrm{T}_1^b(l_1) + R_z(\alpha)K_{bt,2}(u_2(l_1^+) - u_2^*) \tag{57}$$

$$\sum_{i=1}^{2} R_z(\alpha_i)K_{se,i}(v_i(l_1^-) - e_3) = F_1^b(l_1) + R_z(\alpha)K_{se,2}(v_2(l_1^+) - e_3) \tag{58}$$

and the condition at the tip of the robot is as follows:

$$K_{bt,2}(u_2(l_2^-) - u_2^*) = \mathrm{T}_2^b(l_2) \tag{59}$$

$$K_{se,2}(v_2(l_2^-) - e_3) = F_2^b(l_2) \tag{60}$$

where $l_i^{\mp}$ corresponds to the arc-length infinitesimally before and after l_i. A shooting method can be used to find solutions that simultaneously satisfy the constraints on base location and tendon termination loads.

III. Simulation Comparison of Single and Multi-tube Models

The fundamental difference between multiple concentric tendon-actuated tubes and a single tube possessing the same arrangement of tendons is that tendon loading causes the multiple tubes to twist with respect to each other. To illustrate this effect, a single tube with two tendons arranged at 90° to each other is compared with two nested tubes with single tendons rotated so that their tendons are also 90° to each other ($\alpha = 90°$). The nested tubes have the same overall cross section: The single tube has outer and inner diameters of 8 mm and 6 mm. The two tubes have outer and inner diameters of 8 mm and 7 mm (outer) and 7 mm and 6 mm (inner). The tendons are located at radial distances of 3.9 mm and 3.4 mm such that they lie within the individual tubes for the two-tube case. The length of both systems is taken to be 100 mm. A modulus of elasticity (E) of 50 MPa and Poisson's ratio of 0.4 are assumed. As shown in Fig. 3(a), when tension is applied to an individual tendon, the deflections of the single- and two-tube systems are the same. These correspond to the blue tubes lying in the y-z (outer tendon) and x-z planes (outer tendon). This is because both systems possess the same overall bending stiffness and a single tendon does not induce twisting. When tension is applied to both tendons, the single-tube system deflects as shown in red. No twisting occurs, as seen in Fig. 3(b). On the other hand, the individual deflections of the tubes of the two-tube system generate torques on each other similar to precurved concentric tubes. These torques cause the two tubes to twist in opposite directions such that their tendons become more aligned as shown in Fig. 3(b). This causes the tubes to bend more and in a different direction with respect to the z axis.

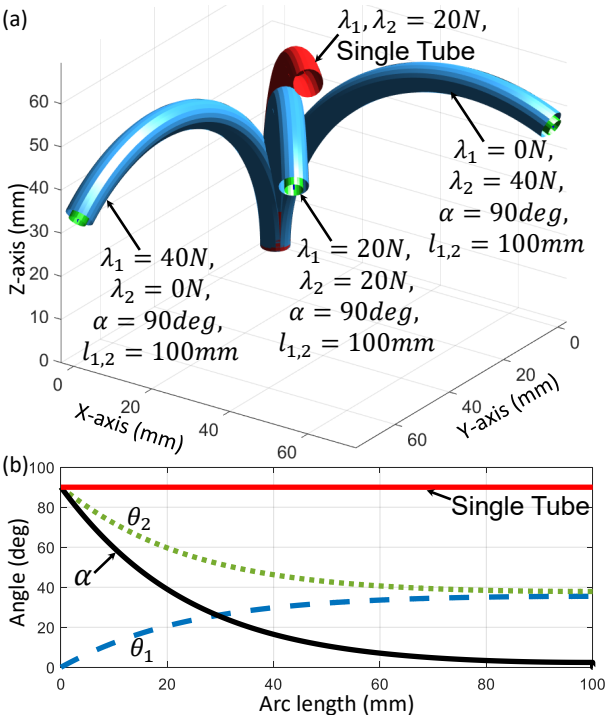

Fig. 3: Comparison of single- and two-tube systems with tendons oriented at 90° to each other. (a) Shapes of systems when single tendons are tensioned and when both are tensioned. (b) Twisting versus arc length for both single- and two-tube systems.

IV. Experimental Model Evaluation

To validate the proposed model, a prototype system comprised of two single-tendon tubes (Fig. 1, Table 1) was used. The tubes are comprised of three layers - an inner layer of PTFE (polytetrafluoroethylene), a braid layer made of Stainless Steel 304, and an outer layer made of PEBAX (a modified polyamide). The tendons run the entire length between the PEBAX and the braid layers. Both tubes are comprised of stiff proximal transmission sections with steerable compliant distal sections. In these experiments, the proximal sections are constrained to remain straight (Fig. 4). Electromagnetic (EM) sensors (Ascension Technology Corp., 3D Guidance trakSTAR, Burlington, VT, USA) with 1.4mm RMS position error were fixed to each tube tip to collect tip position data as shown in Fig. 4. Sensor weight deflection was observed to be negligible.

Data was collected for the 32 configurations corresponding to the combinations of $\alpha \in \{0°, 90°\}$, $\lambda_1 \in \{0, 1, 2\}$ kg, $\lambda_2 \in \{0, 0.5, 1\}$ kg and steerable lengths of $l_1 = 100$ mm and $l_2 = \{100, 150\}$ mm (neglecting configurations with

TABLE I: Two-tube prototype geometric parameters.

Tube	Parameters				
	Transmission Length (mm)	Steerable Distal Length (mm)	ID (mm)	OD (mm)	Tendon Radius (mm)
Outer	730	100	7	8	3.9
Inner	990, 940	100, 150	6	7	3.4

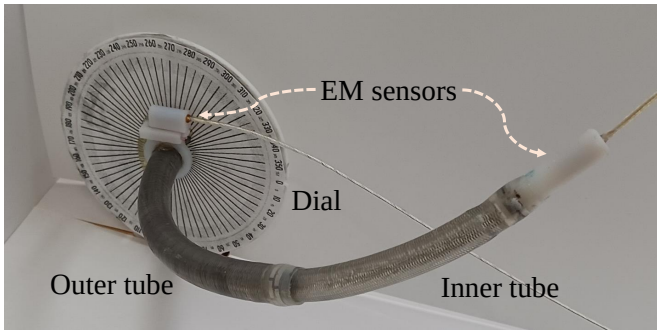

Fig. 4: Experimental prototype testing configuration (shown for $l_1 = 100$ mm, $l_2 = 150$ mm.

$\lambda_1 = \lambda_2 = 0$). Tendons were tensioned by hanging weights via low-friction pulleys. Since the transmission sections experience a small amount of twisting (to be modeled in a future paper) and the values of α were set at the base of the transmission section, the corresponding α values were measured at the base of the steerable section (using an EM sensor and a dial gauge) for use as inputs to the model. To minimize the effect of hysteresis, after each trial, the steerable section was manually straightened.

MATLAB's unconstrained minimization (`fminsearch`) algorithm was used to estimate the constitutive model parameters to minimize mean tip position error between the model and experimental data. Based on our observations of tube anisotropy, separate directional constitutive parameters were included in the minimization: $\{G_{ix}, G_{iy}, G_{iz}, E_{ix}, E_{iy}, E_{iz}\}, i \in \{1, 2\}$. The optimized parameter values are given in Table II.

While the model parameters were fit over all the data (see Fig. 5), modeling error is reported in Table III for the two extension lengths considered separately and also for the total data set. It can be seen that the error increases with robot length. For the complete data set, the mean error of 5.55mm normalized by maximum robot length is 3.7% of the total steerable length. This is comparable to the modeling error observed in other multi-tube continuum robot designs [13], but larger than that of single-tube designs [10].

TABLE II: Optimized Constitutive Model Parameters.

	Parameters					
	E_x (MPa)	E_y (MPa)	E_z (GPa)	G_x (MPa)	G_y (MPa)	G_z (MPa)
Outer	81.93	43.85	10.0	0.71	3.97	27.98
Inner	62.5	62	10.0	9.9	0.43	34.13

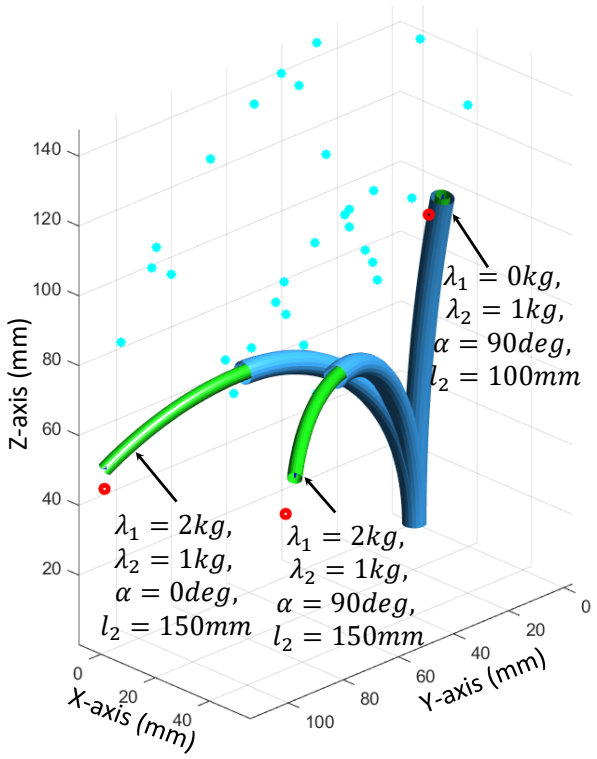

Fig. 5: Model (green and blue tubes) vs. experimental results (red circles and cyan dots). Red circles correspond to depicted model configurations while cyan dots are remaining experimental tip positions used in parameter optimization.

TABLE III: Tip Position Error

Steerable Length	mean $\pm$ std. dev. (mm$\pm$mm)	$\frac{\text{mean error}}{\text{max length}}$ (%)	max (mm)
100 mm	4.03 ± 1.82	4.0	8.01
150 mm	7.07 ± 3.01	4.7	14.22
All data	5.55 ± 2.90	3.7	14.22

V. Conclusion

In this paper, we have introduced a mechanics-based statics model for telescoping tendon-actuated continuum tube robots. Similar to the twisting observed in concentric tube robots fabricated from precurved superelastic tubes, nested tendon-actuated tubes also experience twisting along their length. This phenomenon, which significantly affects overall shape, is captured by the presented model.

Our experimental results indicate that the model can provide mean tip position errors of 3.7% of the steerable length. Owing to the nonlinearity and hysteresis of the polymer construction, maximum modeling error is larger than what is measured in concentric tube robots and in tendon-actuated robots using superelastic central backbones [10], [13]. This accuracy is, however, likely sufficient for robotic control when coupled with sensor-based feedback.

References

[1] P. Dupont, N. Simaan, H. Choset, and C. Rucker, "Continuum robots for medical interventions," *Proceedings of the IEEE*, 2022.

[2] P. E. Dupont, B. J. Nelson, M. Goldfarb, B. Hannaford, A. Menciassi, M. K. O'Malley, N. Simaan, P. Valdastri, and G.-Z. Yang, "A decade retrospective of medical robotics research from 2010 to 2020," *Science Robotics*, vol. 6, no. 60, p. eabi8017, 2021.

[3] A. Al-Ahmad, J. D. Grossman, and P. J. Wang, "Early experience with a computerized robotically controlled catheter system," *Journal of Interventional Cardiac Electrophysiology*, vol. 12, no. 3, pp. 199–202, 2005.

[4] S. Jeong, Y. Chitalia, and J. P. Desai, "Design, modeling, and control of a coaxially aligned steerable (COAST) guidewire robot," *IEEE Robotics and Automation Letters*, vol. 5, no. 3, pp. 4947–4954, 2020.

[5] A. Sarma, T. A. Brumfiel, Y. Chitalia, and J. P. Desai, "Kinematic modeling and jacobian-based control of the coast guidewire robot," *IEEE Transactions on Medical Robotics and Bionics*, vol. 4, no. 4, pp. 967–975, 2022.

[6] M. Sherif, L. Paranskaya, S. Yuecel, S. Kische, O. Thiele, G. D'Ancona, A. Neuhausen-Abramkina, J. Ortak, H. Ince, and A. Öner, "Mitraclip step by step; how to simplify the procedure," *Netherlands heart journal*, vol. 25, no. 2, pp. 125–130, 2017.

[7] A. Agrawal, D. K. Hogarth, and S. Murgu, "Robotic bronchoscopy for pulmonary lesions: a review of existing technologies and clinical data," *Journal of thoracic disease*, vol. 12, no. 6, p. 3279, 2020.

[8] P. Rao, Q. Peyron, S. Lilge, and J. Burgner-Kahrs, "How to model tendon-driven continuum robots and benchmark modelling performance," *Frontiers in Robotics and AI*, vol. 7, p. 223, 2021.

[9] D. B. Camarillo, C. F. Milne, C. R. Carlson, M. R. Zinn, and J. K. Salisbury, "Mechanics modeling of tendon-driven continuum manipulators," *IEEE transactions on robotics*, vol. 24, no. 6, pp. 1262–1273, 2008.

[10] D. C. Rucker and R. J. Webster III, "Statics and dynamics of continuum robots with general tendon routing and external loading," *IEEE Transactions on Robotics*, vol. 27, no. 6, pp. 1033–1044, 2011.

[11] F. Renda and C. Laschi, "A general mechanical model for tendon-driven continuum manipulators," in *2012 IEEE International Conference on Robotics and Automation*. IEEE, 2012, pp. 3813–3818.

[12] K. Hsiao and H. Mochiyama, "A wire-driven continuum manipulator model without assuming shape curvature constancy," in *2017 IEEE/RSJ International Conference on Intelligent Robots and Systems (IROS)*. IEEE, 2017, pp. 436–443.

[13] P. E. Dupont, J. Lock, B. Itkowitz, and E. Butler, "Design and control of concentric-tube robots," *IEEE Transactions on Robotics*, vol. 26, no. 2, pp. 209–225, 2009.

[14] D. C. Rucker, B. A. Jones, and R. J. Webster III, "A geometrically exact model for externally loaded concentric-tube continuum robots," *IEEE transactions on robotics*, vol. 26, no. 5, pp. 769–780, 2010.

[15] E. Amanov, T.-D. Nguyen, and J. Burgner-Kahrs, "Tendon-driven continuum robots with extensible sections—a model-based evaluation of path-following motions," *The International Journal of Robotics Research*, vol. 40, no. 1, pp. 7–23, 2021.

[16] P. S. Gonthina, M. B. Wooten, I. S. Godage, and I. D. Walker, "Mechanics for tendon actuated multisection continuum arms," in *2020 IEEE International Conference on Robotics and Automation (ICRA)*. IEEE, 2020, pp. 3896–3902.